

Improved thermoelectric performance in n-type half-Heusler NbCoSn by heavy-element Pt doping

Federico Serrano-Sánchez¹, Ting Luo², Junjie Yu³, Wenjie Xie⁴, Gudrun Auffermann¹, Anke Weidenkaff⁴, Tiejun Zhu³, Xinbing Zhao³, José A. Alonso⁵, Baptiste Gault², Claudia Felser¹, Chenguang Fu^{1*}

¹Max-Planck-Institut für Chemische Physik fester Stoffe, Nöthnitzer Str. 40, 01187 Dresden, Germany

²Max-Planck-Institut für Eisenforschung GmbH, Max-Planck Straße 1, 40237, Düsseldorf, Germany

³State Key Laboratory of Silicon Materials, School of Materials Science and Engineering, Zhejiang University, 310027 Hangzhou, China

⁴Department of Materials Science, Technical University of Darmstadt, 64287 Darmstadt, Germany

⁵Instituto de Ciencias de Materiales de Madrid (ICMM). Consejo Superior de Investigaciones Científicas (CSIC). Sor Juana Inés de la Cruz 3, 28049, Madrid, Spain

KEYWORDS: Half-Heusler, power factor, grain boundary, synchrotron XRD, SEM

ABSTRACT: Half-Heusler compounds with a valence electron count of 18, including ZrNiSn, ZrCoSb, and NbFeSb, are good thermoelectric materials owing to favourable electronic structures. Previous computational studies had predicted a high electrical power factor in another half-Heusler compound NbCoSn, but it has not been extensively investigated experimentally. Herein, the synthesis, structural characterization, and thermoelectric properties of the heavy-element Pt-doped NbCoSn compounds are reported. Pt is found to be an effective dopant enabling the optimization of electrical power factor, simultaneously leading to a strong point defect scattering of phonons, and thereby suppressing the lattice thermal conductivity. Annealing significantly improves the carrier mobility, which is ascribed to the decreased grain boundary scattering. As a result, a maximum power factor of $\sim 3.4 \text{ mWm}^{-1}\text{K}^{-2}$ is obtained at 600 K. In conjunction with the reduced lattice thermal conductivity, a maximum figure of merit zT of ~ 0.6 is achieved at 773 K for the post-annealed NbCo_{0.95}Pt_{0.05}Sn, an increase of 100% compared to the undoped NbCoSn. This work highlights the important roles of the doping element and microstructure on the thermoelectric properties of half-Heusler compounds.

Introduction

Thermoelectric materials allow the direct conversion of heat into electrical energy. Thermoelectric devices are suitable for various applications owing to a lack of mobile parts, quiet operation, good reliability, endurance, and flexible implementation^{1,2}. Therefore, they have been used for temperature control, power generation, and refrigeration³⁻⁵. The conversion efficiency of a thermoelectric material is determined by its figure of merit, zT , which is calculated from the transport properties, i.e., $zT = \alpha^2 \sigma T / (\kappa_e + \kappa_L)$, where α is the Seebeck coefficient, σ is the electrical conductivity, T is the absolute temperature, and κ_e and κ_L are the electronic and lattice components of thermal conductivity, respectively.

Among the strategies employed to improve the thermoelectric performance of a material, the optimization of carrier concentration (n), usually through chemical doping or defect manipulation, could be the first and foremost one². With this strategy, a large enhancement of zT can be achieved if the initial n of a material deviates significantly from its optimal one. Moreover, band engineering⁶ and hierarchical phonon scattering⁷ are important approaches that can be implemented to further improve the thermoelectric performance^{8,9}. For thermoelectric power generation devices, thermally stable, low-cost, and non-toxic materials are

highly desirable^{8,10}. Fulfilling these requirements, half-Heusler alloys with a valence electron count (VEC) of 18 exhibit good thermoelectric properties at high temperatures^{11,12} and have thus attracted considerable attention for power generation applications^{13,14}. In the half-Heusler alloys, many different strategies have been employed to improve the thermoelectric performance besides carrier concentration optimization, e.g., point defect scattering¹⁵, nanostructuring¹⁶, phase separation¹⁷, band engineering¹⁸, and plastic deformation¹⁹. Consequently, several half-Heusler systems, including (Ti,Zr,Hf)NiSn^{17,20,21}, (Ti,Zr,Hf)CoSb²²⁻²⁴, and (V,Nb,Ta)FeSb^{19,25,26}, have been found to exhibit good zT values of above unity. Half-Heusler alloys with a nominal VEC of 19 have also attracted significant attention, where the intrinsic vacancies play a key role in determining the thermoelectric properties²⁷.

NbCoSn is another half-Heusler alloy with a VEC of 18. The prediction of a large power factor, $\alpha^2 \sigma$, in both n-type and p-type doped NbCoSn indicates promising thermoelectric properties^{28,29}. Particularly, for the p-type NbCoSn, the calculated $\alpha^2 \sigma$ is the largest among all studied half-Heusler alloys²⁸, which might originate from the high degeneracy in the valence band edge³⁰. However, the preparation of a heavily hole-doped NbCoSn is experimentally challenging,

and good thermoelectric performance has not been reported till date. Ti, Mo, and Hf were initially described as weak p-type acceptors for NbCoSn by Kawaharada *et al.*^{31,32} Later, Ferluccio *et al.*³³ reported Zr- and Ti-doped NbCoSn with a positive Seebeck coefficient. Sc was also used as an acceptor for NbCoSn by Yan *et al.*³⁴ However, the low electrical conductivities in these p-type NbCoSn samples suggested that the electrical power factors were not yet optimal, preventing the attainment of the predicted high performance. A possible hindrance in the realization of the heavily hole-doped NbCoSn could be the presence of interstitial Co, predicted to be the most stable intrinsic defect in NbCoSn by Bhattacharya and Madsen²⁹, which could act as a ‘killer-defect’. Excess Co was found in the synthesized NbCoSn samples, despite being designed to have the nominal composition^{34,35}. A similar phenomenon was also observed in the ZrNiSn system, in which excess Ni significantly changes the electronic structure and transport properties^{36,37}. Therefore, further experimental understanding of the intrinsic defect in NbCoSn is necessary to optimize its p-type thermoelectric properties.

Meanwhile, n-type doping has been successfully achieved using Sb as a dopant^{31,33,38}. The alloys of NbCo_{1+x}Sn were prepared by optical floating zone method³⁹. Among these, NbCo_{1.05}Sn showed the highest phase-purity and thermoelectric performance. He *et al.*⁴⁰ reported 80% enhancement in the power factor by improving the samples’ phase purity, resulting in a maximum zT of 0.6 at 973 K in Sb-doped NbCoSn. Additionally, a material comprising the half-Heusler NbCoSn mixed with the full-Heusler NbCo₂Sn was studied, and the antisite disorder was found to be suppressed by annealing⁴¹. Generally, half-Heusler alloys require a high content of chemical doping to realize the optimal electrical power factor and consequently, the dopants could also generate significant suppression on phonon transport¹³. A dopant element with large mass and radius differences compared to the host elements additionally increases phonon scattering, thereby suppressing the lattice thermal conductivity.

In this study, we have prepared heavy-element Pt-doped NbCo_{1-x}Pt_xSn ($x = 0.00–0.15$) samples using arc-melting and high-energy mechanical alloying, followed by a spark plasma sintering (SPS) process. After obtaining the sintered pellets, several samples are further annealed. Laboratory and synchrotron X-ray diffraction (XRD) measurements show that the obtained samples possess pure half-Heusler phases with negligible secondary phases. Heavy-element Pt doping leads to the simultaneously improved power factor and suppressed lattice thermal conductivity. Post-annealing is effective in decreasing the grain boundary scattering of carriers and thus, contributes to a high mobility. As a result, a maximum zT of ~ 0.6 is obtained at 773 K for the post-annealed NbCo_{0.95}Pt_{0.05}Sn, which is the highest value for this system at this temperature.

Experimental

In the first set of the experiments, stoichiometric amounts of Nb slug (99.95%, Alfa Aesar), Co slug (99.95%, Alfa Aesar), Sn shot (99.999%, Alfa Aesar), and Pt shot (99.9%) with compositions of NbCo_{1-x}Pt_xSn ($x = 0.00, 0.03, 0.06, 0.09, 0.12$, and 0.15) were weighed and loaded in a water-cooled

Cu crucible of the arc-melter to prepare 4.5 g of each sample. Each pellet was melted three times under an inert Ar atmosphere to guarantee homogenization. To remove the residual impurities, the samples were annealed at 1073 K for seven days inside vacuum-sealed quartz ampoules using Ta foil to minimise the oxidation. Subsequently, the samples were ground using a ball-milling machine (Pulverisette 7, Fritsch), after which the resulting powders were compacted under inert conditions using SPS. The powders were placed in a 10-mm cylindrical graphite die and a uniaxial pressure of 80 MPa was applied while heating rapidly to 1223 K and then kept for 5 min. Then, the sintered pellets were used for the characterization of structural and transport properties. In the second set of experiments, two additional NbCo_{1-x}Pt_xSn samples were prepared with $x = 0.05$ and 0.1 . To improve the phase purity, these two samples were additionally annealed for seven days at 1073 K after the SPS process.

XRD was performed at room temperature using an image-plate Huber G670 Guinier camera equipped with a Ge(111) monochromator and employing Co K α_1 radiation. Synchrotron XRD (SXRD) patterns were collected with an incident beam of 28 keV energy ($\lambda = 0.4427 \text{ \AA}$), in the high angular resolution mode (MAD set-up) on the MSPD-diffractometer at the ALBA synchrotron in Barcelona, Spain. The ground samples were analysed using quartz capillaries with 0.25-mm radius. Rietveld refinements of XRD and SXRD patterns were performed using FullProf program^{42,43}. A pseudo-Voigt function was employed for analysing the shapes of the diffraction peaks. There were no excluded regions in the refinements. The final refinement of the synchrotron data was performed using parameters such as scale factor, set of background points, zero-point shift, pseudo-Voigt shape, and isotropic thermal displacement parameters of Nb, Co/Pt, and Sn.

Microstructural analysis of the samples was performed using scanning electron microscopy (SEM, Zeiss Merlin scanning electron microscope, Carl Zeiss AG, Oberkochen, Germany) in the backscattered mode, at an accelerating voltage of 30 kV and a beam current of 2 nA.

High-temperature measurements of the Seebeck coefficient and electrical resistivity were performed using an ULVAC-RICO ZEM-3 equipment. The thermal conductivity was calculated using the equation, $\kappa = C_p D \rho$, where C_p is the specific heat, D is the thermal diffusivity, and ρ is the sample density, employing thermal diffusivity values measured by a LASER Flash (LFA 457, Netzsch). C_p is calculated using the formula, $C_p = C_{ph,H} + C_D$, where $C_{ph,H}$ and C_D are the contributions of the harmonic phonons and lattice dilation, respectively, which can be calculated by employing the sound velocity, thermal expansion coefficient, and density (Table S1, supporting information)²⁴.

The Hall effect measurements were performed in sample rods in a four-probe configuration using the resistivity option of the physical property measurement system (PPMS, Quantum Design). The measurements were symmetrised to eliminate the magnetoresistance contribution, and the carrier concentration was calculated using the formula, $R_H = -1/en_H$, where R_H is the Hall coefficient, e is the free electron charge, and n_H is the Hall carrier concentration.

Results and Discussion

The laboratory XRD patterns of the two sets of $\text{NbCo}_{1-x}\text{Pt}_x\text{Sn}$ ($x = 0.00-0.15$) samples are shown in Figure 1a. The main phase is consistent with the cubic MgAgAs -type half-Heusler structure, and tiny impurity peaks are hardly observed in the range of binary phases (Nb_3Sn , Co_7Nb_6) typically reported for this compound⁴¹. Although the impurity peaks are more noticeable for the samples with high Pt contents, the peak intensities are very low to enable precise identification of these secondary phases using the laboratory XRD analysis. Moreover, despite further annealing of the samples with $x = 0.05$ and $x = 0.10$ in the second set of experiments for seven days at 1073 K, no marked difference in the phase purity is observed compared to those of the other samples from the first set of experiments. To perform a more detailed analysis of the structure and phase purity, high-resolution SXRD experiments were carried out for samples with $x = 0.00$ and $x = 0.05$ from the first and second sets of experiments, respectively. The crystalline structure corresponds to the $F\bar{4}3m$ space group, with Nb atoms located at 4a (0,0,0), Co/Pt at 4c (1/4,1/4,1/4), and Sn at 4b (1/2,1/2,1/2) Wyckoff positions. The refinements yield good agreement factors (Table S2, supporting information), while the isotropic displacement parameters are slightly higher than those described by neutron diffraction due to the effects of radiation absorption^{33,41}. The accurate calculation of the occupation factors to analyze the defects as off-stoichiometry or antisite defects is not possible owing to the highly symmetric positions of the atoms and the absorption effects. The full Heusler phase is not detected, and very weak intensity peaks are observed in the $9-11^\circ$ range corresponding to an extremely low volume fraction of the secondary impurity phases (Figures 1b and 1c). Overall, the high-resolution SXRD measurements also suggest no marked differences in the phase purities for the samples with $x = 0.00$ and $x = 0.05$, despite the higher Pt content and post-annealing of the latter.

Lattice parameters (Figure 1d) were determined using Rietveld refinements of the XRD patterns in the $F\bar{4}3m$ space group, displaying an excellent match with the literature data³³. The lattice parameter value increases almost linearly with an increase in the Pt content, which indicates the efficiency of Pt as a donor for NbCoSn . Carrier concentration measurements allow the assessment of the effectiveness of Pt doping in terms of the electron transfer to the half-Heusler structure. Figure 1d shows a linear behaviour with an increase in the dopant concentration, and similar values have been reported for slightly higher Sb dopant concentrations⁴⁰. Using a simple assumption of one added electron per Pt atom, the estimations of the carrier concentrations (red dashed line in Figure 1d) are consistent with the experimental values. However, carrier concentration is an integral measurement for a bulk sample, and the contribution of the possible micro- or nanoscale features within the material is compounded in the measured value. The calculated carrier concentration is $9.42 \times 10^{20} \text{ cm}^{-3}$ for $x = 0.05$, which is close to the experimental value. The results indicate that Pt is a highly effective dopant for this system.

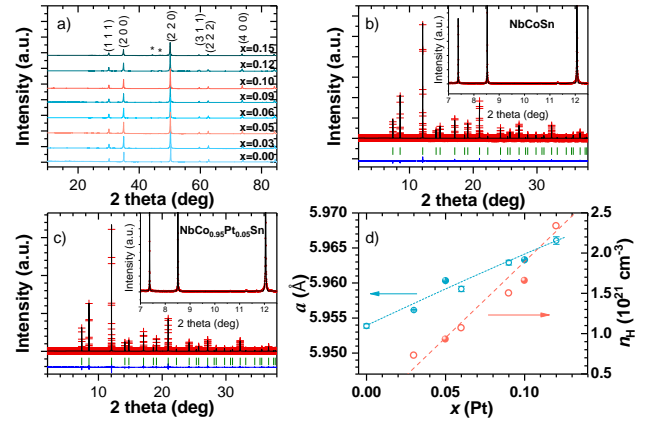


Figure 1. a) Indexed laboratory XRD patterns of $\text{NbCo}_{1-x}\text{Pt}_x\text{Sn}$ ($x = 0.00-0.15$). Rietveld refinement of synchrotron XRD patterns using $\lambda = 0.4427 \text{ \AA}$ at room temperature with experimental (red crosses), calculated (black line), difference (blue line), and Bragg reflections (green segments) of NbCoSn (b) and the post-annealed $\text{NbCo}_{0.95}\text{Pt}_{0.05}\text{Sn}$ (c), displaying an almost complete absence of impurities in the inset (magnified image) in the typical 2θ range. d) Lattice parameters for $\text{NbCo}_{1-x}\text{Pt}_x\text{Sn}$ ($x = 0.00, 0.03, 0.06, 0.09, 0.12$, and 0.15) represented by empty blue circles, and post-annealed $\text{NbCo}_{1-x}\text{Pt}_x\text{Sn}$ ($x = 0.05, 0.10$) represented by filled blue circles. Blue dashed line is a guide for the eye. Carrier concentration is represented by red empty and filled circles. The red dashed line denotes the carrier concentration calculated using one added electron per Pt atom.

The temperature-dependence of the electronic conductivity σ for $\text{NbCo}_{1-x}\text{Pt}_x\text{Sn}$ ($x = 0.00-0.15$) samples is shown in Figure 2a. An increasing trend is observed for the pristine NbCoSn sample, indicating a semiconducting behaviour. After doping with Pt, the σ value shows a noticeable increase in the complete temperature range, with a decreasing trend at temperatures above 500 K, suggesting a degenerate semiconductor behaviour. Interestingly, the sample with $x = 0.05$, which is post-annealed, shows a higher σ compared to that of the sample with $x = 0.06$, despite the higher carrier concentration of the latter. A similar phenomenon is also observed for the other post-annealed sample with $x = 0.10$, whose σ value at room temperature is higher than that of the sample with $x = 0.12$. Thereafter, the carrier mobilities of the samples were calculated (Figure 2b). Overall, the two post-annealed samples with $x = 0.05$ and $x = 0.10$ have higher carrier mobilities than those of the others, suggesting an annealing-induced change in the microstructure. Therefore, the backscattered SEM measurements were performed for samples with $x = 0.05$ and $x = 0.06$, as shown in Figures 2c and 2d, respectively. This analysis shows that the sample with $x = 0.05$, with post-annealing after SPS, has a grain size of a few micrometres, which is almost ten times larger than that of the sample with $x = 0.06$. Grain boundary scattering has recently been found to hinder the mobilities and conductivities (particularly near room temperature) of Mg_3Sb ⁴⁴, half-Heusler $\text{Nb}_{1-x}\text{Ti}_x\text{FeSb}$ ⁴⁵ and $(\text{Zr}, \text{Hf})\text{CoSb}$ ⁴⁶, and elemental Te ^{47,48}. Herein, an increase in the grain size in post-annealed samples can support their high electrical conductivities and carrier mobilities. The confirmation of the influence of grain boundary processes will be the focus of a separate study.

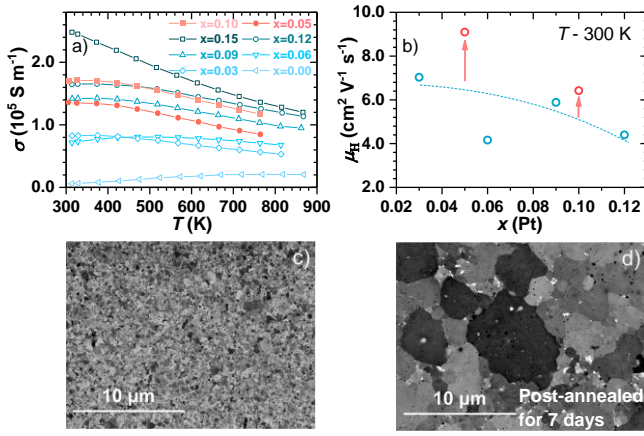


Figure 2. a) Temperature dependence of the electrical conductivity of $\text{NbCo}_{1-x}\text{Pt}_x\text{Sn}$ ($x = 0.00-0.15$). b) Carrier mobility as a function of the Pt content, where the dashed blue line is a guide for the eye. Backscattered SEM images of c) $\text{NbCo}_{0.94}\text{Pt}_{0.06}\text{Sn}$ and d) the post-annealed $\text{NbCo}_{0.95}\text{Pt}_{0.05}\text{Sn}$.

The temperature dependence of the Seebeck coefficient (Figure 3a) of Pt-doped samples shows the typical behaviour of a degenerated semiconductor. The absolute Seebeck coefficient increases in the complete temperature range with no observable contribution from bipolar conduction. In contrast, the pristine NbCoSn shows an increase in the Seebeck coefficient up to 600 K, when a small bump is observed. Similar data have been previously reported for the undoped compound^{33,39}. As expected according to the Pisarenko relationship⁹, the absolute Seebeck coefficient decreases with an increase in the dopant content due to the increased electron concentration.

A Pisarenko plot using the single parabolic band model²⁴ (Figure 3b) was used to better assess the electrical properties of n-type NbCoSn . A density of state effective mass m^* of $6.5 m_e$ is derived for the Pt-doped NbCoSn samples. Notably, this m^* value is close to that of the n-type $(\text{Zr,Hf})\text{CoSb}$ ^{24,46,49}, but more than two times higher than that of n-type $(\text{Zr,Hf})\text{NiSn}$ ^{20,50}. As both n-type $(\text{Zr,Hf})\text{CoSb}$ and $(\text{Zr,Hf})\text{NiSn}$ have a band degeneracy of 3, and the calculated electronic structure of NbCoSn shows a higher band degeneracy of 6²⁸⁻³⁰, the band effective mass of NbCoSn is lower than that of $(\text{Zr,Hf})\text{CoSb}$, but still higher than that of $(\text{Zr,Hf})\text{NiSn}$.

The variation in calculated power factor is shown in Figure 3c. It follows an increasing trend with an increase in temperature because of an increase in the absolute Seebeck coefficient up to 600–700 K and then saturates at high temperatures due to the decreased electrical conductivity. Pt doped NbCoSn samples exhibit noticeably higher power factors than that of the undoped NbCoSn , suggesting the optimization of electrical properties. Moreover, the second set of samples with $x = 0.05$ and $x = 0.10$, which have larger grain sizes, show overall higher power factors than those of the first set of samples. This is attributed to the decreased grain scattering and thus improved carrier mobility. A maximum power factor of $\sim 3.4 \text{ mW m}^{-1} \text{ K}^{-2}$ is obtained at 600 K for the post-annealed sample with $x = 0.05$, which is comparable to that of $\text{NbCoSn}_{0.9}\text{Sb}_{0.1}$ at 900 K⁴⁰.

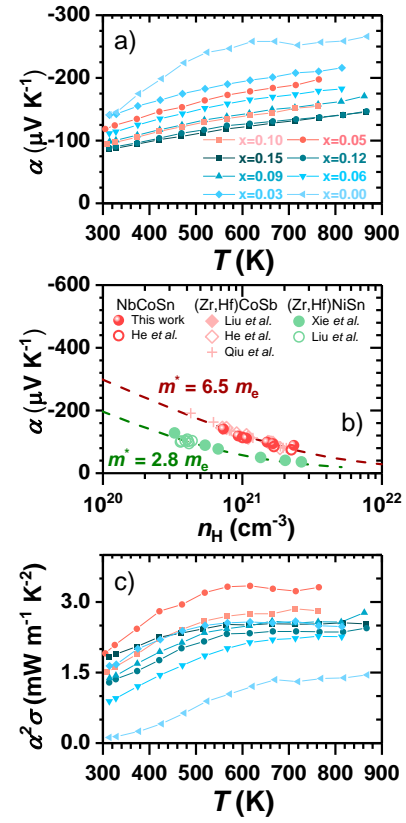


Figure 3. a) Temperature dependence of Seebeck coefficient for $\text{NbCo}_{1-x}\text{Pt}_x\text{Sn}$ ($x = 0.00-0.15$). b) Pisarenko plot at room temperature for several n-type half-Heusler compounds including NbCoSn ⁴⁰, $(\text{Zr,Hf})\text{CoSb}$ ^{24,46,49}, and $(\text{Zr,Hf})\text{NiSn}$ ^{20,50}. c) Temperature dependence of power factor for $\text{NbCo}_{1-x}\text{Pt}_x\text{Sn}$ ($x = 0.00-0.15$).

The change in total thermal conductivity κ of $\text{NbCo}_{1-x}\text{Pt}_x\text{Sn}$ with temperature is shown in Figure 4a. A decrease in the κ value of Pt-doped samples is observed near room temperature. To further understand this behaviour, κ_e and κ_L were calculated using the equations, $\kappa_e = L\sigma T$ and $\kappa_L = \kappa - \kappa_e$, where L is the Lorenz number and calculated using the single parabolic band model²⁴. As shown in Figure 4b, a notable decrease in κ_L is observed upon Pt-doping and a maximum reduction of 45% is obtained for $x = 0.15$, indicating that heavy element doping is effective in enhancing the phonon scattering by introducing strong mass and strain field fluctuations¹³. This reduction is almost linearly related to the Pt content as observed in Figure 4c, regardless of the grain sizes of the samples, suggesting that point defects dominate the phonon scattering while the grain boundaries might not significantly affect the phonon transport. At a high Pt content, κ_L shows lower values than those previously reported for this system, typically in the range of 5–10 $\text{W m}^{-1} \text{ K}^{-1}$ at room temperature^{33,40,41}. In addition, an increase in κ_e is observed with an increase in the Pt content because of an increase in the electrical conductivity. Compared to Sb doping⁴⁰, Pt doping is more effective at suppressing the κ_L of NbCoSn , thereby contributing to the decrease in κ . These values are comparable and even lower than those obtained

for the NbCoSn–NbCoSb solid-solutions, in which the disorder and Nb vacancies have a strong impact on the phonon conduction³³.

Owing to the simultaneously decreased κ_L and improved power factor, Pt doping is effective in improving the figure of merit zT of NbCoSn (Figure 4d). A 100% increase in the peak zT is observed for NbCo_{0.95}Pt_{0.05}Sn, compared to that for NbCoSn, leading to a maximum value of ~ 0.6 at 773 K. This value is similar to that for Sb-doped NbCoSn system but occurs at a lower temperature. Furthermore, the almost linear temperature dependence of zT in all the studied NbCo_{1-x}Pt_xSn samples suggests that a higher peak zT can be achieved at higher temperatures.

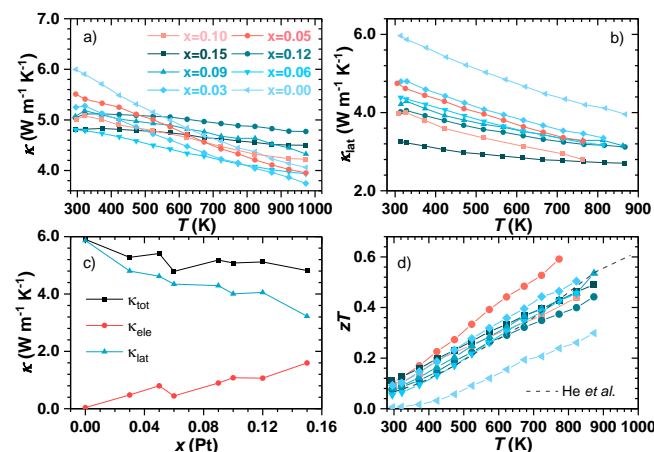


Figure 4. Temperature evolution of a) total thermal conductivity and b) lattice thermal conductivity. c) Variation of κ , κ_e , and κ_L with an increase in Pt content at room temperature. d) Figure of merit zT for NbCo_{1-x}Pt_xSn ($x = 0.00$ – 0.15) as a function of temperature. zT for the optimised NbCoSn_{0.95}Sb_{0.1} is also shown⁴⁰.

Conclusions

In summary, heavy-element Pt-doped NbCoSn alloys are successfully prepared *via* arc-melting and high-energy mechanical alloying followed by SPS. The structure and thermoelectric properties are systematically characterized. Pt is found to be an effective dopant for NbCoSn, leading to the simultaneously improved electrical and thermal transport properties, thereby resulting in enhanced thermoelectric performance. Post-annealing is effective in decreasing the grain boundary scattering of carriers and thus contributes to a high carrier mobility. A maximum power factor of ~ 3.4 mWm⁻¹K⁻² is obtained at 600 K. Furthermore, the lattice thermal conductivity is significantly decreased due to the enhanced point defect scattering of phonons, and a direct relationship between the doping content and this reduction is observed. A peak zT of 0.6 at 773 K is obtained for the post-annealed NbCo_{0.95}Pt_{0.05}Sn, which is comparable to the highest reported value and can be further improved at high temperatures. This work highlights the importance of the selection of doping elements and microstructure in improving the thermoelectric properties of half-Heusler compounds.

ASSOCIATED CONTENT

Supporting Information.

Calculated heat capacity, coefficient of linear thermal expansion, electronic contribution to thermal conductivity, structural parameters of Rietveld refinement of SXRD patterns. This material is available free of charge via the Internet at <http://pubs.acs.org>.

AUTHOR INFORMATION

Corresponding Author

*Chenguang.Fu@cpfs.mpg.de

Author Contributions

The manuscript was written through contributions of all authors. All authors have given approval to the final version of the manuscript.

Note

The authors declare no competing financial interest.

ACKNOWLEDGMENT

This work was funded by the Deutsche Forschungsgemeinschaft (DFG, German Research Foundation) – Projektnummer (392228380), the ERC Advanced Grant No. 742068 “TOPMAT”, and the National Natural Science Foundation of China (no. 51761135127). F. Serrano acknowledges financial support by the Spanish Ministry of Economy and Competitiveness through grant MAT2017-84496-R and the European Union’s Horizon 2020 research and innovation program under the Marie Skłodowska-Curie grant agreement No 839821. Dr. T. Luo is grateful for the financial support from the Alexander von Humboldt Stiftung. We thank ALBA synchrotron (Barcelona, Spain) for providing the SXRD beam time. A. W. and W. X. acknowledge the financial support from Deutsche Forschungsgemeinschaft (Project No. BA 4171/4-1).

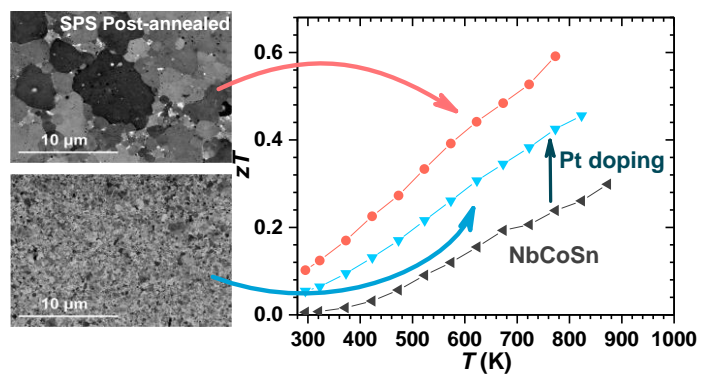
REFERENCES

- (1) Rowe, D. M. Thermoelectrics, an Environmentally-Friendly Source of Electrical Power. *Renew. Energy* **1999**, *16*, 1251–1256.
- (2) Snyder, G. J.; Toberer, E. S. Complex Thermoelectric Materials. *Nat. Mater.* **2008**, *7*, 105–114.
- (3) Russ, B.; Glaudell, A.; Urban, J. J.; Chabinyc, M. L.; Segalman, R. A. Organic Thermoelectric Materials for Energy Harvesting and Temperature Control. *Nat. Rev. Mater.* **2016**, *1*, 16050.
- (4) He, R.; Schierning, G.; Nielsch, K. Thermoelectric Devices: A Review of Devices, Architectures, and Contact Optimization. *Adv. Mater. Technol.* **2018**, *3*, 1700256.
- (5) Barnhart, T. R.; Ranalli, M.; Adldinger, M. Temperature Control Systems with Thermoelectric Devices. U.S. Patent No. 9,447,994, September 20, 2016.
- (6) Pei, Y.; Shi, X.; LaLonde, A.; Wang, H.; Chen, L.; Snyder, G. J. Convergence of Electronic Bands for

- High Performance Bulk Thermoelectrics. *Nature* **2011**, *473*, 66–69.
- (7) Biswas, K.; He, J.; Blum, I. D.; Chun-IWu; Hogan, T. P.; Seidman, D. N.; Dravid, V. P.; Kanatzidis, M. G. High-Performance Bulk Thermoelectrics with All-Scale Hierarchical Architectures. *Nature* **2012**, *489*, 414–418.
 - (8) He, J.; Tritt, T. M. Advances in Thermoelectric Materials Research: Looking Back and Moving Forward. *Science (80-.)* **2017**, *357*, eaak9997.
 - (9) Zhu, T.; Liu, Y.; Fu, C.; Heremans, J. P.; Snyder, J. G.; Zhao, X. Compromise and Synergy in High-Efficiency Thermoelectric Materials. *Adv. Mater.* **2017**, *29*.
 - (10) Rull-Bravo, M.; Moure, A.; Fernández, J. F.; Martín-González, M. Skutterudites as Thermoelectric Materials: Revisited. *RSC Adv.* **2015**, *5*, 41653–41667.
 - (11) Graf, T.; Felser, C.; Parkin, S. S. P. Simple Rules for the Understanding of Heusler Compounds. *Prog. Solid State Chem.* **2011**, *39*, 1–50.
 - (12) Zhu, T.; Fu, C.; Xie, H.; Liu, Y.; Zhao, X. High Efficiency Half-Heusler Thermoelectric Materials for Energy Harvesting. *Adv. Energy Mater.* **2015**, *5*, 1500588.
 - (13) Fu, C.; Bai, S.; Liu, Y.; Tang, Y.; Chen, L.; Zhao, X.; Zhu, T. Realizing High Figure of Merit in Heavy-Band p-Type Half-Heusler Thermoelectric Materials. *Nat. Commun.* **2015**, *6*, 8144.
 - (14) Xing, Y.; Liu, R.; Liao, J.; Zhang, Q.; Xia, X.; Wang, C.; Huang, H.; Chu, J.; Gu, M.; Zhu, T. High-Efficiency Half-Heusler Thermoelectric Modules Enabled by Self-Propagating Synthesis and Topologic Structure Optimization. *Energy Environ. Sci.* **2019**, *12*, 3390–3399.
 - (15) Yang, J.; Meisner, G. P.; Chen, L. Strain Field Fluctuation Effects on Lattice Thermal Conductivity of ZrNiSn-Based Thermoelectric Compounds. *Appl. Phys. Lett.* **2004**, *85*, 1140–1142.
 - (16) Xie, W.; Weidenkaff, A.; Tang, X.; Zhang, Q.; Poon, J.; Tritt, T. M. Recent Advances in Nanostructured Thermoelectric Half-Heusler Compounds. *Nanomaterials* **2012**, *2*, 379–412.
 - (17) Schwall, M.; Balke, B. Phase Separation as a Key to a Thermoelectric High Efficiency. *Phys. Chem. Chem. Phys.* **2013**, *15*, 1868–1872.
 - (18) Fu, C.; Zhu, T.; Liu, Y.; Xie, H.; Zhao, X. Band Engineering of High Performance P-Type FeNbSb Based Half-Heusler Thermoelectric Materials for Figure of Merit $ZT > 1$. *Energy Environ. Sci.* **2015**, *8*, 216–220.
 - (19) Rogl, G.; Ghosh, S.; Wang, L.; Bursik, J.; Grytsiv, A.; Kerber, M.; Bauer, E.; Mallik, R. C.; Chen, X.-Q.; Zehetbauer, M. Half-Heusler Alloys: Enhancement of ZT after Severe Plastic Deformation (Ultra-Low Thermal Conductivity). *Acta Mater.* **2020**, *183*, 285–300.
 - (20) Liu, Y.; Xie, H.; Fu, C.; Snyder, G. J.; Zhao, X.; Zhu, T. Demonstration of a Phonon-Glass Electron-Crystal Strategy in (Hf, Zr) NiSn Half-Heusler Thermoelectric Materials by Alloying. *J. Mater. Chem. A* **2015**, *3*, 22716–22722.
 - (21) Rogl, G.; Sauerschnig, P.; Rykavets, Z.; Romaka, V. V.; Heinrich, P.; Hinterleitner, B.; Grytsiv, A.; Bauer, E.; Rogl, P. (V, Nb)-Doped Half Heusler Alloys Based on {Ti, Zr, Hf} NiSn with High ZT. *Acta Mater.* **2017**, *131*, 336–348.
 - (22) Yan, X.; Liu, W.; Wang, H.; Chen, S.; Shiomi, J.; Esfarjani, K.; Wang, H.; Wang, D.; Chen, G.; Ren, Z. Stronger Phonon Scattering by Larger Differences in Atomic Mass and Size in P-Type Half-Heuslers Hf 1– x Ti x CoSb 0.8 Sn 0.2. *Energy Environ. Sci.* **2012**, *5*, 7543–7548.
 - (23) Rausch, E.; Balke, B.; Ouardi, S.; Felser, C. Enhanced Thermoelectric Performance in the P-Type Half-Heusler (Ti/Zr/Hf) CoSb 0.8 Sn 0.2 System via Phase Separation. *Phys. Chem. Chem. Phys.* **2014**, *16*, 25258–25262.
 - (24) Liu, Y.; Fu, C.; Xia, K.; Yu, J.; Zhao, X.; Pan, H.; Felser, C.; Zhu, T. Lanthanide Contraction as a Design Factor for High-Performance Half-Heusler Thermoelectric Materials. *Adv. Mater.* **2018**, *30*, 1–7.
 - (25) Yu, J.; Fu, C.; Liu, Y.; Xia, K.; Aydemir, U.; Chasapis, T. C.; Snyder, G. J.; Zhao, X.; Zhu, T. Unique Role of Refractory Ta Alloying in Enhancing the Figure of Merit of NbFeSb Thermoelectric Materials. *Adv. Energy Mater.* **2018**, *8*, 1701313.
 - (26) Zhu, H.; Mao, J.; Li, Y.; Sun, J.; Wang, Y.; Zhu, Q.; Li, G.; Song, Q.; Zhou, J.; Fu, Y. Discovery of TaFeSb-Based Half-Heuslers with High Thermoelectric Performance. *Nat. Commun.* **2019**, *10*, 1–8.
 - (27) Xia, K.; Liu, Y.; Anand, S.; Snyder, G. J.; Xin, J.; Yu, J.; Zhao, X.; Zhu, T. Enhanced Thermoelectric Performance in 18-Electron Nb_{0.8}CoSb Half-Heusler Compound with Intrinsic Nb Vacancies. *Adv. Funct. Mater.* **2018**, *28*, 1–7.
 - (28) Yang, J.; Li, H.; Wu, T.; Zhang, W.; Chen, L.; Yang, J. Evaluation of Half-Heusler Compounds as Thermoelectric Materials Based on the Calculated Electrical Transport Properties. *Adv. Funct. Mater.* **2008**, *18*, 2880–2888.
 - (29) Bhattacharya, S.; Madsen, G. K. H. A Novel P-Type Half-Heusler from High-Throughput Transport and Defect Calculations. *J. Mater. Chem. C* **2016**, *4*, 11261–11268.
 - (30) Dylla, M. T.; Dunn, A.; Jain, A.; Snyder, G. J. Machine Learning Chemical Guidelines for Engineering Electronic Structures in Half-Heusler Thermoelectric Materials.
 - (31) KAWAHARADA, Y.; KUROSAKI, K.; MUTA, H.;

- UNO, M.; YAMANAKA, S. High Temperature Thermoelectric Properties of $\text{CoNb}_{1-x}\text{Hf}_x\text{Sn}_{1-y}\text{Sb}_y$ Half-Heusler Compounds. *J. Alloys Compd.* **2004**, *377*, 312–315.
- (32) Kawaharada, Y.; Kurosaki, K.; Muta, H.; Uno, M.; Yamanaka, S. High Temperature Thermoelectric Properties of $\text{CoNb}_{1-x}\text{M}_x\text{Sn}$ Half-Heusler Compounds. *J. Alloys Compd.* **2004**, *384*, 303–307.
- (33) Ferluccio, D. A.; Smith, R. I.; Buckman, J.; Bos, J. W. G. Impact of Nb Vacancies and P-Type Doping of the NbCoSn - NbCoSb Half-Heusler Thermoelectrics. *Phys. Chem. Chem. Phys.* **2018**, *20*, 3979–3987.
- (34) Yan, R.; Xie, W.; Balke, B.; Chen, G.; Weidenkaff, A. Realizing p-Type NbCoSn Half-Heusler Compounds with Enhanced Thermoelectric Performance via Sc Substitution. *Sci. Technol. Adv. Mater.* **2020**, *21*, 122–130.
- (35) Li, S.; Zhu, H.; Mao, J.; Feng, Z.; Li, X.; Chen, C.; Cao, F.; Liu, X.; Singh, D. J.; Ren, Z. N-Type TaCoSn -Based Half-Heuslers as Promising Thermoelectric Materials. *ACS Appl. Mater. Interfaces* **2019**, *11*, 41321–41329.
- (36) Zeier, W. G.; Schmitt, J.; Hautier, G.; Aydemir, U.; Gibbs, Z. M.; Felser, C.; Snyder, G. J. Engineering Half-Heusler Thermoelectric Materials Using Zintl Chemistry. *Nat. Rev. Mater.* **2016**, *1*, 16032.
- (37) Fu, C.; Yao, M.; Chen, X.; Maulana, L. Z.; Li, X.; Yang, J.; Imasato, K.; Zhu, F.; Li, G.; Auffermann, G. Revealing the Intrinsic Electronic Structure of 3D Half-Heusler Thermoelectric Materials by Angle-Resolved Photoemission Spectroscopy. *Adv. Sci.* **2020**, *7*, 1902409.
- (38) Ono, Y.; Inayama, S.; Adachi, H.; Kajitani, T. Thermoelectric Properties of NbCoSn -Based Half-Heusler Alloys. In *2006 25th International Conference on Thermoelectrics*; 2006; pp 124–127.
- (39) Kimura, Y.; Tamura, Y.; Kita, T. Thermoelectric Properties of Directionally Solidified Half-Heusler Compound NbCoSn Alloys. *Appl. Phys. Lett.* **2008**, *92*, 2–5.
- (40) He, R.; Huang, L.; Wang, Y.; Samsonidze, G.; Kozinsky, B.; Zhang, Q.; Ren, Z. Enhanced Thermoelectric Properties of N-Type NbCoSn Half-Heusler by Improving Phase Purity. *APL Mater.* **2016**, *4*.
- (41) Buffon, M. L. C.; Laurita, G.; Verma, N.; Lamontagne, L.; Ghadbeigi, L.; Lloyd, D. L.; Sparks, T. D.; Pollock, T. M.; Seshadri, R. Enhancement of Thermoelectric Properties in the Nb-Co-Sn Half-Heusler/Heusler System through Spontaneous Inclusion of a Coherent Second Phase. *J. Appl. Phys.* **2016**, *120*.
- (42) Rietveld, H. M. A Profile Refinement Method for Nuclear and Magnetic Structures. *J. Appl. Crystallogr.* **1969**, *2*, 65–71.
- (43) Rodríguez-Carvajal, J. Recent Advances in Magnetic Structure Determination by Neutron Powder Diffraction. *Phys. B* **1993**, *192*, 55–69.
- (44) Imasato, K.; Fu, C.; Pan, Y.; Wood, M.; Kuo, J. J.; Felser, C.; Snyder, G. J. Metallic N-Type Mg_3Sb_2 Single Crystals Demonstrate the Absence of Ionized Impurity Scattering and Enhanced Thermoelectric Performance. *Adv. Mater.* **2020**, 1908218.
- (45) He, R.; Kraemer, D.; Mao, J.; Zeng, L.; Jie, Q.; Lan, Y.; Li, C.; Shuai, J.; Kim, H. S.; Liu, Y. Achieving High Power Factor and Output Power Density in P-Type Half-Heuslers $\text{Nb}_{1-x}\text{Ti}_x\text{FeSb}$. *Proc. Natl. Acad. Sci.* **2016**, *113*, 13576–13581.
- (46) Qiu, Q.; Liu, Y.; Xia, K.; Fang, T.; Yu, J.; Zhao, X.; Zhu, T. Grain Boundary Scattering of Charge Transport in N-Type (Hf, Zr) CoSb Half-Heusler Thermoelectric Materials. *Adv. Energy Mater.* **2019**, *9*, 1803447.
- (47) Wu, Y.; Zhang, Q.; Liu, F.; Fang, T.; Zhu, T.; Zhao, X. Scattering Mechanisms and Compositional Optimization of High-Performance Elemental Te as a Thermoelectric Material. *Adv. Electron. Mater.* **2020**, *2000038*, 1–11.
- (48) Wu, Y.; Liu, F.; Zhang, Q.; Zhu, T.; Xia, K.; Zhao, X. B. Enhancing Average Thermoelectric Figure of Merit of Elemental Te by Suppressing the Grain Boundary Scattering. *J. Mater. Chem. A* **2020**.
- (49) He, R.; Zhu, H.; Sun, J.; Mao, J.; Reith, H.; Chen, S.; Schierning, G.; Nielsch, K.; Ren, Z. Improved Thermoelectric Performance of N-Type Half-Heusler $\text{MCo}_{1-x}\text{Ni}_x\text{Sb}$ (M= Hf, Zr). *Mater. Today Phys.* **2017**, *1*, 24–30.
- (50) Xie, H.; Wang, H.; Pei, Y.; Fu, C.; Liu, X.; Snyder, G. J.; Zhao, X.; Zhu, T. Beneficial Contribution of Alloy Disorder to Electron and Phonon Transport in Half-Heusler Thermoelectric Materials. *Adv. Funct. Mater.* **2013**, *23*, 5123–5130.

Table of Contents



Supporting Information

Improved thermoelectric performance in n-type half-Heusler NbCoSn by heavy-element Pt doping

Federico Serrano-Sánchez¹, Ting Luo², Junjie Yu³, Wenjie Xie⁴, Gudrun Auffermann¹, Anke Weidenkaff⁴, Tiejun Zhu³, Xinbing Zhao³, José A. Alonso⁵, Baptiste Gault², Claudia Felser¹, Chenguang Fu^{1*}

¹Max-Planck-Institut für Chemische Physik fester Stoffe, Nöthnitzer Str. 40, 01187 Dresden, Germany

²Max-Planck-Institut für Eisenforschung GmbH, Max-Planck Straße 1, 40237, Düsseldorf, Germany

³State Key Laboratory of Silicon Materials, School of Materials Science and Engineering, Zhejiang University, 310027 Hangzhou, China

⁴Department of Materials Science, Technical University of Darmstadt, 64287 Darmstadt, Germany

⁵Instituto de Ciencias de Materiales de Madrid (ICMM). Consejo Superior de Investigaciones Científicas (CSIC). Sor Juana Inés de la Cruz 3, 28049, Madrid, Spain

Table S1. Calculated and Dulong-Petit specific heat, longitudinal and transversal sound velocities, coefficient of linear thermal expansion (CLTE) and density for $x = 0.05$ and $x = 0.10$ Pt-doped NbCoSn.

Composition	Calc. C_p @300 K ($Jg^{-1}K^{-1}$)	DP C_p ($Jg^{-1}K^{-1}$)	v_l (ms^{-1})	v_t (ms^{-1})	CLTE ($10^{-6} K^{-1}$)	ρ (gcm^{-3})
NbCo_{0.95}Pt_{0.05}Sn	0.252	0.269	5563	3028	9.14	8.64 (99.2%)
NbCo_{0.9}Pt_{0.1}Sn	0.246	0.263	5471	2906	10.7	8.75 (98.3%)

Figure S1. Calculated heat capacity from CLTE compared to Dulong-Petit value of Pt-doped NbCoSn.

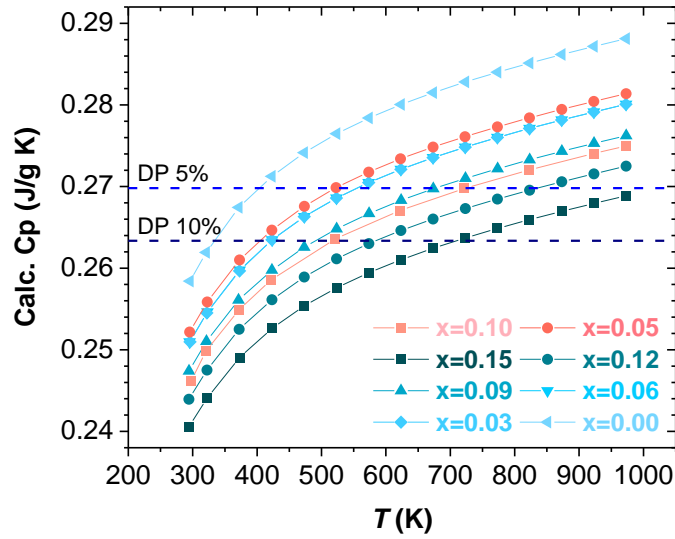


Figure S2. Electronic contribution to thermal conductivity of Pt-doped NbCoSn.

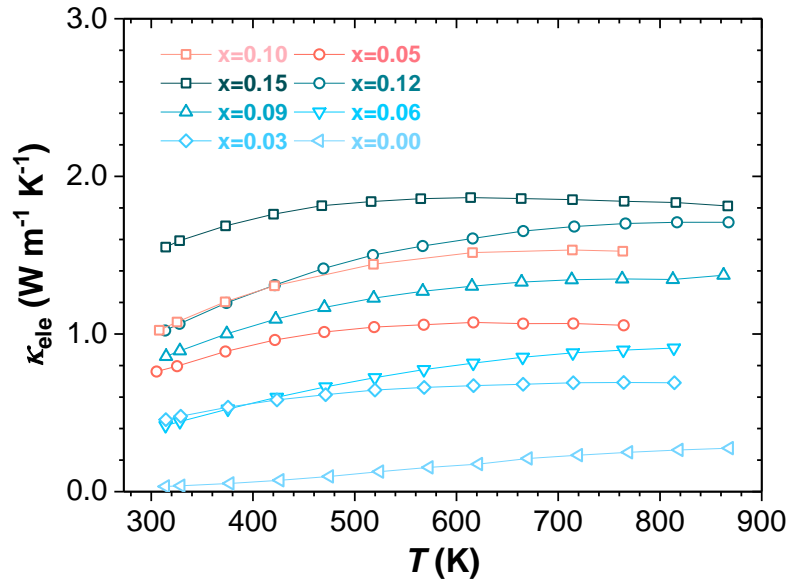


Table S2. Structural parameters of NbCoSn and NbCo_{0.95}Pt_{0.05}Sn obtained by Rietveld refinement of Synchrotron XRD patterns.

Composition	NbCoSn	NbCo _{0.95} Pt _{0.05} Sn
Latt.parameter a/Å	5.95386(4)	5.96556(3)
V/Å³	211.055(2)	212.3020(17)
U_{iso}, Nb/Å²	0.0018(16)	0.0041(13)
U_{iso}, Co/Pt/Å²	0.0054(7)	0.0065(6)
U_{iso}, Sn /Å²	0.0098(18)	0.0106(14)
R_i	3.15	2.06
R_p	6.18	9.42
R_{wp}	7.72	12.3
R_{exp}	4.97	7.27
χ²	2.41	2.87